

Notes and Correspondence

The movement of Indian monsoon depressions by interaction with image vortices near the Himalayan wall

Kieran M. R. Hunt^{a*} and Douglas J. Parker^b

^aDepartment of Meteorology, University of Reading, UK

^bSchool of Earth and Environment, University of Leeds, UK

*Correspondence to: K. M. R. Hunt, Department of Meteorology, University of Reading, PO Box 243 Reading, RG6 6BB, UK.
E-mail: k.hunt@pgr.reading.ac.uk

It is argued that a simple explanation for the westward propagation of Indian monsoon depressions (IMDs) is the interaction of the depression vortex with the Himalayan ‘wall’. This interaction can be modelled by simulating an IMD as a point vortex in a horizontal plane (at 850 hPa) and invoking image vortices behind the barrier. Solenoidal flows associated with the image vortices allow the boundary conditions at the Himalayas to be met, and cause the IMD vortex to propagate parallel to the barrier, toward the west. This simple model is tested against propagation speeds for observed IMDs. The histogram of observed propagation speed, normalised by the point-vortex model prediction, has a mean of 1.08 and standard deviation of 0.68. The model also explains the observed intensification of flow on the Himalayan side of the IMD which is a key process in enhancing rainfall to the Indo-Gangetic Plain in the monsoon season.

Key Words: monsoon; depressions; Himalayas; vortices; India

Received 20 January 2015; Revised 28 March 2016; Accepted 3 April 2016; Published online in Wiley Online Library 13 June 2016

1. Introduction

Indian monsoon depressions (IMDs) are the most important synoptic-scale features of the summer rainy season over the Indian subcontinent. Typically they have their genesis over the northern Bay of Bengal, before propagating towards the west, parallel to the Himalayan massif, and against the direction of the climatological mean flow (Figure 1). Although the forecasting of these systems is of profound importance, due to the enhanced rainfall which they bring during the monsoon season, their dynamics remain relatively poorly understood. In particular, their basic mode of propagation, against the mean flow, has not until recently been adequately explained. Boos *et al.* (2015) have presented the movement of IMDs in terms of the advection of the potential vorticity maximum at 450–500 hPa, above the IMD core. At these levels the mean flow is more clearly easterly and the PV structure of the IMD can be seen to be advected by the local flow, which includes an additional northwestward component from adiabatic potential vorticity beta drift, rather than the previously established theory of quasi-geostrophic lifting and downshear vortex stretching (Sanders, 1984; Chen *et al.*, 2005).

Here we propose another, probably complementary first-order explanation for the direction and speed of propagation of IMDs, in terms of the interaction of their vorticity structure at low levels with the neighbouring ‘wall’, represented by the Himalayas. We approximate the Indian Monsoon Depression (IMD) as a point

vortex in two-dimensional flow. Whilst baroclinic processes play a significant rôle in monsoon depressions (Krishnamurti, 1985), a barotropic model remains a good approximation, if we assume the depression winds do not vary much with height in the lower troposphere and that temperature is not advected. This is justifiable because most of the relative vorticity of an IMD is confined to a small region at its centre (Godbole, 1977; Hunt *et al.*, 2016). Two-dimensional flow is only strictly accurate for systems in which horizontal divergence is small and vorticity generation by stretching is weak relative to advection. Monsoon depressions are typically tall and narrow, with high Burger number ($Bu = NH/fL$, where H and L are vertical and horizontal length-scales, and f is the Brunt–Väisälä frequency), meaning that the influence of their potential vorticity structure on the ambient flow should be dominated by horizontal circulation rather than vertical stratification (e.g. Hoskins and James, 2014, p. 339). However, vorticity tendencies due to stretching remain significant (Boos *et al.*, 2015). Previous authors (Krishnamurti, 1985) have shown that baroclinic effects in monsoon depressions are in fact strong, and undoubtedly the effects of deep convection in the monsoon system introduce significant vorticity tendencies in the environment of a monsoon depression. Therefore we must see the 2D model as a highly idealised system, which neglects some important tendencies related to vorticity generation by stretching, but from which we can nevertheless hope to build dynamical insight into certain physical processes.

Invoking this approximation, we define the point-vortex vorticity field:

$$\omega = \kappa \cdot \delta(x - x_v) \delta(y - y_v), \tag{1}$$

where κ is the circulation, δ is the Dirac delta-function, and (x_v, y_v) is the location of the vortex. The circulation, κ , around a point vortex, vorticity ω , is given by:

$$\kappa = \oint_{\partial S} \mathbf{v} \cdot d\mathbf{l} = \iint_S \omega \cdot d\mathbf{S}, \tag{2}$$

where \mathbf{v} is the flow velocity vector field, $d\mathbf{l}$ is an element of the closed line boundary ∂S to the surface S through which the vorticity vectors pass, and $d\mathbf{S} = \mathbf{n}dS$, where \mathbf{n} is the unit vector normal to S . In the case of a point vortex in two-dimensional flow (the approximation to which we will consider), S is chosen to be coplanar with the fluid.

To represent interaction with the orography, we make an approximation of the Himalayas as a vertical plane (normal to the surface) and impose the resulting boundary condition of no-normal flux. We can make use of the standard result (e.g. Batchelor, 2000) that such a boundary condition is satisfied by replacing the plane with an equal and opposite image vortex (of strength $-\kappa$), whose location is the point of reflection of the original vortex in that plane. If the projection of the vertical plane onto the surface is given by $ax + by + c = 0$, then the location of the required image vortex is $-\{(by_v + c)/a, (ax_v + c)/b\}$. The resulting flow around each vortex causes the other vortex to be advected parallel to the wall, as indicated in Figure 2. We also note the intensification of winds on the ‘Himalayan’ side of the vortex. This appears to be at variance with the findings of Godbole (1977), who found that winds to the south of the depression centre were stronger than to the north; however, this discrepancy is reconciled immediately when we subtract the background monsoonal flow, as shown in Figure 3. This flow exhibits a strong meridional shear which significantly amplifies westerlies south of the IMD centre.

The velocity field due to each point vortex is

$$\begin{bmatrix} u \\ v \end{bmatrix} = \frac{\kappa}{2\pi r^2} \begin{bmatrix} -(y - y_j) \\ (x - x_j) \end{bmatrix}, \tag{3}$$

where $r = \sqrt{(x - x_j)^2 + (y - y_j)^2}$ is the distance from vortex j . Thus, in the absence of background flow, our point-vortex representation of an IMD will propagate westwards, parallel to the Himalayas, at a speed

$$v_l = \kappa/4\pi R, \tag{4}$$

where R is the distance between the vortex and boundary representing the mountains. Incorporating the existence of a background flow (Figure 1), \mathbf{v}_{flow} , gives the following expression:

$$\frac{|\mathbf{v} - \mathbf{v}_{\text{flow}}|}{v_l} = 1, \tag{5}$$

where we have introduced the notation \mathbf{v} for the propagation vector of the vortex. Therefore, if an IMD behaves like a point vortex adjacent to the Himalayan ‘wall’, the expression on the left of Eq. (5) should evaluate to 1.

By examining the rôle played by the Himalayas in the general presence of depressions (Figure 4), it could be argued that the shape of the Himalayan wall shows significant curvature and may be better approximated by a cylinder than by a simple plane intersecting the horizontal level. The motion of a point vortex adjacent to a cylindrical barrier can also be computed using image vortices, using the method of Milne-Thomson (1940) (described in Batchelor, 2000), and in this case two image vortices are needed; one of strength κ at the centre of the cylinder, and one of strength $-\kappa$ at an image point of the real vortex, inside the cylinder. From

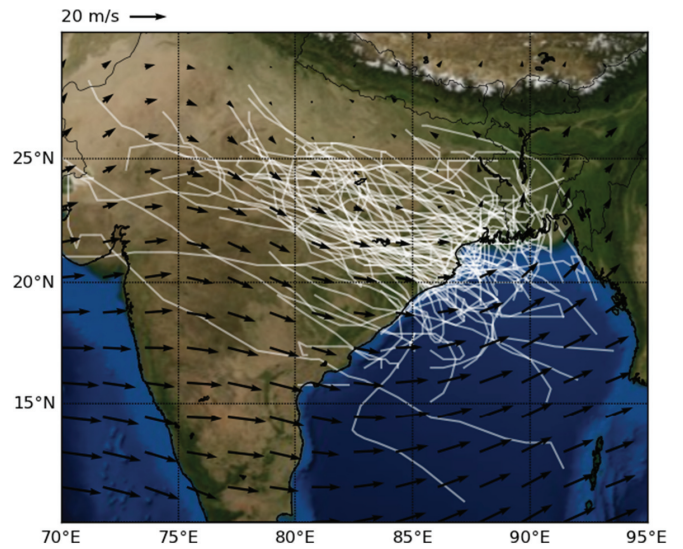


Figure 1. Mean boreal summer (JJAS) 850 hPa wind vectors with Indian monsoon depression tracks 1979–2013 overlaid in white.

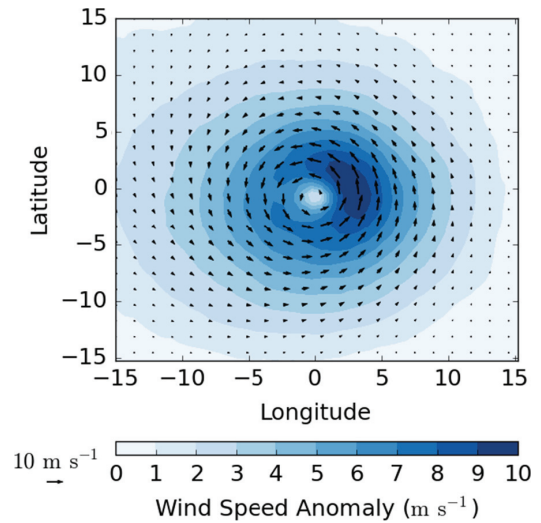


Figure 2. Flow around a pair of counter-rotating ideal point vortices, identical to an ideal point vortex, V , and its corresponding image vortex, I , in the image plane (grey).

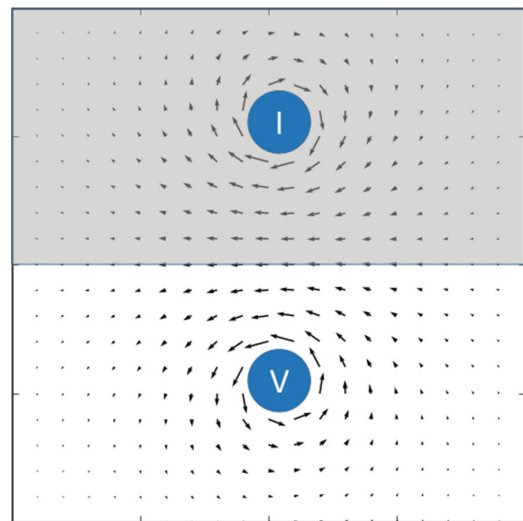


Figure 3. Composite 850 hPa IMD winds with the boreal summer climatology subtracted (from Hunt *et al.*, 2016). In this composite, the data for individual time steps are rotated such that the direction of propagation is due north (up the page) and translated such that the centre is at 0°N, 0°W on a regular lat/lon grid. Therefore, here the Himalayas lie to the right.

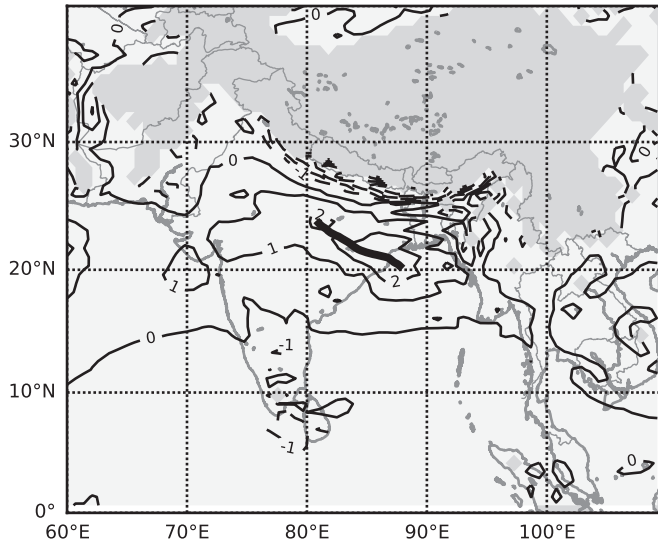


Figure 4. Modified from Hunt *et al.* (2016), 850 hPa relative vorticity (intervals of 10^{-5} s^{-1} , dashed contours are negative) on June–September depression days as an anomaly to the boreal summer mean; greyed out where the orography is higher than the 850 hPa level. The thick black line represents the average path of tracked depressions.

these we obtain the following relationship for the motion of the point vortex:

$$\frac{|\mathbf{v} - \mathbf{v}_{\text{flow}}|}{v_{\text{cyl}}} = 1, \quad (6)$$

and

$$v_{\text{cyl}} = v_1 \cdot \left\{ \left(1 + \frac{r}{a} \right) \left(1 + \frac{r}{2a} \right) \right\}^{-1}, \quad (7)$$

where a is the radius of curvature of the cylinder. A full derivation is given in the Appendix. Therefore, this correction factor for curvature of the Himalayan wall acts to reduce the resulting speed of the point vortex.

2. Data and methods

Hunt *et al.* (2016) devised an objective feature-based tracking algorithm to collect and analyse data on Indian monsoon depressions. They used ERA-Interim reanalysis data (Dee *et al.*, 2011) to locate local 850 hPa relative vorticity maxima and removed those not associated with nearby surface pressure lows. They subsequently imposed the India Meteorological Department (Saha *et al.*, 1981; Krishnamurthy and Ajayamohan, 2010) criterion that monsoon depressions must have surface wind speeds above 8.5 m s^{-1} and not exceeding 16.5 m s^{-1} , and linked events occurring in adjacent timesteps using a nearest-neighbour approach. Finally they filtered out those events not present within the India Meteorological Department's own IMD eAtlas (http://www.imdchennai.gov.in/cyclone_eatlas.htm; accessed 25 April 2016). This results in the rejection of some candidates, and a slightly different database of IMDs compared to those of other studies (e.g. Hurley and Boos, 2015). Whilst it is beyond the scope of this study to intercompare such datasets, a broad majority of events are shared between them and a superficial investigation into the composite structures of IMDs suggests that there is no significant difference between datasets. Indeed, in the subsequent analysis, the results differ by no more than a few percent between the IMDs in Hurley and Boos (2015) and Hunt *et al.* (2016).

For the purposes of calculating circulation, relative vorticity data were collected from the 850 hPa level, as that is where the vorticity and wind speed maxima tend to occur (Hunt *et al.*, 2016). We have used 1-arcminute resolution data from ETOPO1 (<https://www.ngdc.noaa.gov/mgg/global/global.html>; accessed 25 April 2016) to find the regions within the southern

Himalayan foothills where the orography rises above 850 hPa (1.5 km). For the sake of the linear model, a least-squares linear regression of these points suggests that the linear Himalayan wall has a direction parallel with 282° ; for the cylindrical model, a least-squares circle fit gives the wall a radius of curvature of 2570 km centred at 89.1°N , 44.7°E . Note that here, and throughout this study, we measure direction as a bearing clockwise from due north (i.e. due west is 270°).

For each six-hourly timestep of reanalysis data that contained an IMD, we define the propagation vector as the mean velocity vector connecting the present IMD location with its location in the previous timestep (i.e. if the depression has travelled 3.6 km due west during the previous 6 h, its propagation vector will have magnitude 1 m s^{-1} * and direction 270°). We also define the climatological 850 hPa wind vector co-located with the depression centre by taking the value of 21-day running mean wind fields (analogous to the method of Hurley and Boos, 2015) at the location of the IMD centre. Resolving the climatological wind vector onto the direction of the propagation vector (i.e. computing $|\mathbf{v}_{\text{flow}}| \cdot \cos(\alpha)$, where \mathbf{v}_{flow} is the climatological wind vector and α is the difference in angle between \mathbf{v}_{flow} and \mathbf{v} , the propagation vector) for each timestep gives a mean value of -3.15 m s^{-1} ; this indicates that IMDs generally travel in a direction opposing the ambient flow. This indicates the importance of including $|\mathbf{v} - \mathbf{v}_{\text{flow}}|$ in our calculations.

For comparison with our model, we present three simple alternative models: a climatological model and a pair of beta-drift models. For the climatological model, which is intended as a basic benchmark for variability, we simply make the assumption that all IMDs at all times travel at the average IMD velocity (that is to say, we take the mean propagation vector, 1.66 m s^{-1} on 332° , and assert that all IMDs should have this velocity at all timesteps).

For the beta-drift models, we assume that IMDs propagate as cyclones advecting higher-latitude planetary vorticity from the north to west of the centre. We therefore expect that, if IMDs propagated using this mechanism, they should also travel northwestward. There are then two options, both of which are carried out here, when considering the background wind: we either include it directly in the calculation (referred to hereafter as 'beta drift + flow') or we subtract it from the result (referred to hereafter as 'beta drift')[†]. For these, we shall use a modified Rankine vortex of the form:

$$v_\theta(r) = \begin{cases} C_1 r & \text{if } r < r_m, \\ C_2 r^{-\sigma} & \text{if } r \geq r_m, \end{cases} \quad (8)$$

$$v_r(r) = -\lambda v_\theta, \quad (9)$$

where C_1 and C_2 are arbitrary constants related to intensity, r is the distance from the centre, σ is a structure parameter, λ is a horizontal convergence parameter, r_m is the radius of maximum wind speed, and v_θ and v_r are the azimuthal (clockwise positive) and radial (outward positive) components of wind speed respectively. For the IMDs in our dataset (1526 six-hourly timesteps over 106 depressions), the value of the convergence parameter is typically positive (as expected) but close to zero, averaging 0.06 with a standard deviation of 0.18; the structure parameter has an average of 0.83 and a standard deviation of 1.59, compared with 0.5 to 0.6 for tropical cyclones (Leslie and Holland, 1995), and exactly 1 for the point vortex. Both parameters were calculated for each timestep by using logarithmic and linear regressions respectively for the reanalysis gridpoints in the region $r_m < r < 2r_m$. Then, following Holland (1982), the direction of propagation θ_m due to beta drift in the absence of background

*The propagation speed for each IMD timestep is actually calculated by dividing the great circle distance between its start and end points by its duration (6 h).

[†]To clarify, this is different from the mechanism proposed by Boos *et al.* (2015), which is horizontal nonlinear advection of the mid-level (500 hPa) potential vorticity maximum.

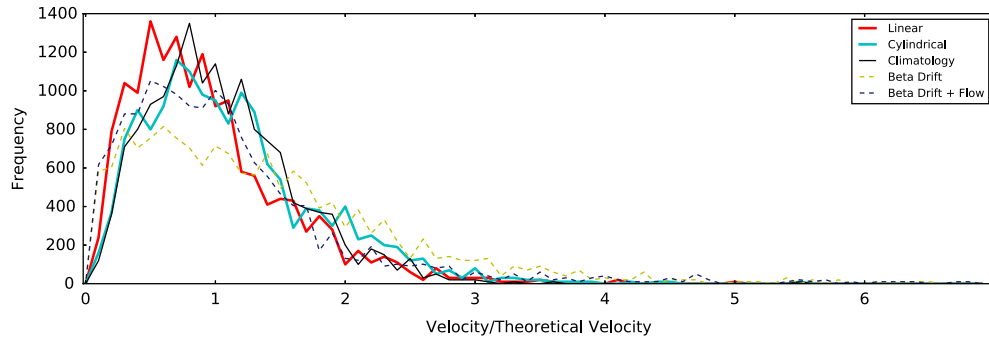


Figure 5. Histogram showing the ratio of observed to predicted IMD propagation velocities for each of the five models discussed in the text calculated for all timesteps present in the dataset. Thick lines represent our linear and cylindrical models respectively; thin black represents a simple model based on the climatology; dashed lines represent a simple beta drift model (not) including background monsoonal flow.

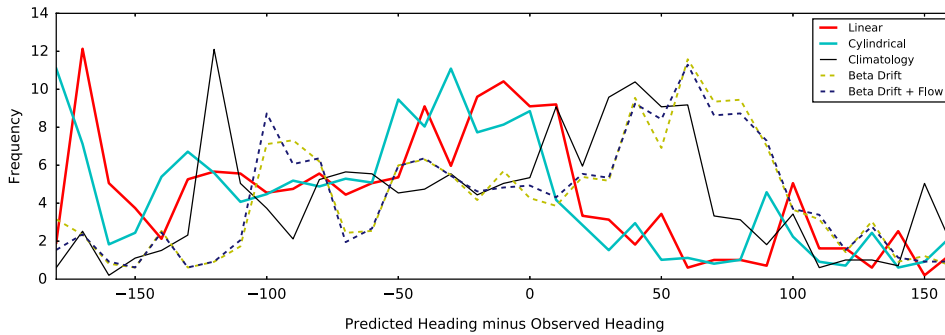


Figure 6. As Figure 5, but showing the difference between the predicted heading and the observed heading.

flow (as measured clockwise from due north), is given by

$$\theta_m = \arctan \left\{ \frac{1}{\lambda(2 - \sigma)} \right\}, \quad (10)$$

and the subsequent drift velocity, v_m , by

$$v_m = \frac{\beta r^2}{1 - \sigma^2} \{ \sin \theta_m + \lambda(2 - \sigma) \cos \theta_m \}, \quad (11)$$

where $\beta = \partial f / \partial y$ is the standard notation for rate of change of the Coriolis parameter with increasing meridional distance. Again, following Holland (1982), this can be adapted to include the effect of a local background flow with velocity v_b and direction (defined, like θ_m , as the angle measured counterclockwise from due north) θ_b :

$$\theta_d = \arctan \left\{ \frac{\frac{1 - \sigma^2}{r^2} v_b \sin \theta_b + \beta}{\frac{1 - \sigma^2}{r^2} v_b \cos \theta_b + \lambda(2 - \sigma)\beta} \right\}, \quad (12)$$

and

$$v_d = v_b \cos(\theta_d - \theta_b) + \frac{\beta r^2}{1 - \sigma^2} \{ \sin \theta_d + \lambda(2 - \sigma) \cos \theta_d \}. \quad (13)$$

An important caveat here is that, if IMDs really were exact point vortices, they would not propagate using this mechanism because $v_b \rightarrow \infty$ as $\sigma \rightarrow 1$.

3. Results

We start by considering the distribution of velocities for IMDs in the period considered. The average IMD speed is 4.24 m s^{-1} with standard deviation 3.1 m s^{-1} , and the average heading is 332° . When the velocities are normalised (Figure 5), both point-vortex models perform well. The cylindrical model, with a mean normalised speed of 1.08 and standard deviation of 0.68, slightly outperforms the linear model, with a mean of 0.90 and standard deviation of 0.61, in that it predicts the propagation speed with marginally better accuracy, but higher variance.

Figures 5 and 6 show, respectively, distributions of the speed and angle predictions from each model compared to reality.

Table 1. Means and standard deviations of the normalised predicted velocity, $|v - v_{\text{flow}}|/v_{\text{model}}$, and the error in predicted heading, $\theta_{\text{actual}} - \theta_{\text{model}}$, for each of the five models.

Model	$\overline{\left(\frac{ v - v_{\text{flow}} }{v_{\text{model}}} \right)}$	St. Dev.	$\overline{\theta_{\text{actual}} - \theta_{\text{model}}}$	St. Dev.
Linear	0.90	0.61	-37.8°	84.8°
Cylin.	1.08	0.68	-23.3°	88.3°
Clim.	1.00	0.56	0.0°	80.7°
BD	1.35	1.28	10.6°	82.2°
BDF	1.14	1.25	14.1°	81.6°

Cylin. = Cylindrical, Clim. = Climatology, BD = Beta drift, BDF = Beta drift + flow.

Table 1 tabulates the means and standard deviations of each. We see that, in predicting velocity, our linear and cylindrical models perform well – both have markedly lower variance than either of the beta drift models and predict the propagation velocity very accurately. Both beta drift models and the linear model struggle to predict the lowest observed velocities (not shown), but the cylindrical model and climatology predict these somewhat more accurately. Further, both beta drift models suffer badly with underprediction (i.e. high values of $(|v - v_{\text{flow}}|)/v_{\text{model}}$, beyond the right edge of the frequency distribution in Figure 5) of IMD speed in quite a number of cases. As a comparison metric, we propose computing the fraction of the 1526 pairs of data from the two distributions in Figures 5 and 6 that, when used to predict the location of an IMD (by extrapolating the diagnosed velocity), travelling at 3 m s^{-1} , 24 h in advance, are correct to within 100 km – the approximate radius of the area of heavy surface rainfall (Hunt *et al.*, 2016). The calculated success rates were, in descending order: cylindrical -0.296 , climatological -0.280 , linear -0.274 , beta drift -0.215 , beta drift + flow -0.195 . If we expand this to bootstrapping 10 000 random unmatched pairs, the performance of the linear and cylindrical models drop (the other three do not), resulting in the climatological model scoring most highly. This strongly implies that these two models at least partially describe the propagation mechanism, and that the cylindrical model performs best overall.

A two-tailed Student's *t*-test confirmed that the means for the linear and cylindrical model results were significantly different at

the 99% confidence level. However, both of our models have some small systematic error in predicting the propagation direction, giving it a northward bias. To reiterate, the values given for standard deviation are dimensionless, as are those for the mean.

It is known that monsoon depressions exist in other areas, notably Australia and Central Africa (Hurley and Boos, 2015). In these locations, the depressions also exist over land, but do not have significant orography with which to interact; therefore we might assume that they would propagate poleward and westward less frequently if the mechanism proposed in this study were correct. Using the global database of depressions outlined in Hurley and Boos (2015), we found that Indian monsoon depressions propagate westward and poleward significantly more frequently than those in either the Australian or African basins, and more rapidly than those in the Australian basin. African monsoon depressions propagated westward most rapidly of all, likely owing to the strong environmental easterlies at around 650 hPa in the African Easterly Jet. This dominates the organisation of African Easterly Waves in that region, and closed depressions are not particularly common there – systems exist mostly as open waves with a maximum amplitude at the jet level.

4. Conclusions

From these results it seems that a simple, first-order explanation for the propagation of IMD vortices is that of the model of a point vortex interacting with the ‘cylindrical wall’ of the Himalayas. Figure 5 shows that the mean speed of vortices is very close to the value predicted by this model, with standard deviation $\sim 1.0 \text{ m s}^{-1}$ (cf. $\sim 1.1 \text{ m s}^{-1}$ for actual IMDs).

Departures from this model ($|\mathbf{v} - \mathbf{v}_{\text{flow}}|/v_{\text{cyl}}$) have standard deviation 0.68 (Figure 5). This could be partly due to errors in our calculations (finite size of vortex, vortex maximised at another level etc.), but also we can assume that other physical and dynamical processes will influence the movement of real IMDs from case to case. Such processes include upper-level interactions and diabatic effects. There may be more boundary-layer friction for vortices close to the mountains. The image vortex causes an irrotational deformation flow acting on the real vortex. In reality, this deformation flow exists to satisfy the correct boundary condition imposed by the mountains. We should expect forecast models to capture this very well.

Boos *et al.* (2015) showed how IMD movement can be inferred through the advection of the 450 hPa PV maximum in the IMD by the local flow at that level, which is enhanced by beta drift, in which the PV anomalies induced by the meridional flow around the vortex generate a meridional northwestward advection of the vortex. Our arguments relating to the advection of the 850 hPa vortex maximum are probably complementary to the results of Boos *et al.* (2015), in that we invoke the advection of the IMD structure, rather than wave-propagation mechanisms presented by earlier authors. Boos *et al.* (2015) also show how the alignment of the 500 hPa PV structure with that at 700 hPa can explain the upwind advection of the MD PV at the lower level. On average, the 500 hPa PV lies to the southwest of the 700 hPa potential vortex, and is consistent with shifting the 700 hPa circulation field to the southwest of the PV at that level. In consequence, the circulation induced at 700 hPa by the 500 hPa PV acts to advect the 700 hPa PV toward the northwest, as observed. Boos *et al.* (2015) note that a Rossby scale height for these systems is typically 2.3 km, meaning that this vertical influence of the 500 hPa PV will be significantly weaker at 850 hPa, but it remains likely that some influence will be felt. Quite likely, the topographic effects of the Himalayas described in this article, which will be strongest in the lower levels, combine constructively in the vertical to produce systematic advection to the northwest throughout the lower troposphere, and to maintain the vertical alignment of the monsoon depressions as described by Boos *et al.* (2015) and Hunt *et al.* (2016). It would be reasonable now to state that the

PV maximum of an IMD is advected westwards by the local wind in the mid-troposphere (modified by beta drift) while its low-level structure also moves westward, against the mean wind at this level, due to interaction with image vortices behind the Himalayan barrier. For these reasons, the dynamics of MDs are probably unique worldwide.

The intensification of the flow on the Himalayan side of the vortex, as observed in real IMDs, is generated by the sum of flows from the IMD and its image, and will act to enhance the southeasterly recurvature of the monsoonal winds from the Bay of Bengal. The presence of the mountains, or equivalently the image vortex, increases the moisture advection in the Indo-Gangetic Plain and is an important factor in the amplification of rainfall by IMDs within the monsoon season.

Acknowledgements

KMRH receives partial support from the Met Office under the aegis of the NERC CASE studentship scheme, and is also supported by the NERC grant NE/L501608/1. DJP has been supported in this work by the INCOMPASS Project (NERC NE/L013843/1) and the Met Office Academic Partnership. The authors wish to thank Prof. Bill Boos and another, anonymous, reviewer for their invaluable critique and suggestions to improve this work.

Appendix

Derivation of cylindrical model propagation velocity

This derivation loosely follows the method outlined in Milne-Thomson (1960). We start by invoking the definition of a meromorphic complex velocity potential function, w :

$$w \equiv w(z) = \phi(z) + i\psi(z), \quad (\text{A1})$$

where ϕ is the velocity potential that describes irrotational flow in the fluid, ψ is the stream function that describes its solenoidal flow, and $z = x + iy = re^{i\theta}$ is the complex coordinate. A rectilinear vortex filament centred at z_ω then has the complex potential

$$w = i\omega \ln(z - z_\omega) = \frac{i\kappa}{2\pi} \ln(z - z_\omega), \quad (\text{A2})$$

where ω and κ are, respectively, the vorticity and circulation of the vortex.

Now consider a two-dimensional inviscid fluid on an infinite plane. This fluid satisfies the generic form

$$w = f(z). \quad (\text{A3})$$

If we impinge upon this flow a cylinder whose cross-section is described by the boundary $|z| = a$, the resulting complex potential becomes

$$w = f(z) + \bar{f}\left(\frac{a^2}{z}\right), \quad (\text{A4})$$

as long as there are no singularities in $f(z < a)$; for a proof, the reader is encouraged to study Milne-Thomson (1940).

Thus, combining Eqs (A2) and (A4), we deduce that the complex potential for a fluid containing a point vortex at z_ω and a cylinder, radius $|a|$, centred at the origin is

$$w = i\omega \ln(z - z_\omega) - i\omega \ln\left(\frac{a^2}{z} - \bar{z}_\omega\right), \quad (\text{A5})$$

or, to within a constant,

$$w = i\omega \ln(z - z_\omega) - i\omega \ln\left(z - \frac{a^2}{\bar{z}_\omega}\right) + i\omega \ln(z), \quad (\text{A6})$$

and in polar coordinates:

$$w = i\omega \left\{ \ln(re^{i\theta} - r_\omega e^{i\theta_\omega}) - \ln\left(re^{i\theta} - \frac{a^2}{r_\omega} e^{i\theta_\omega}\right) + \ln(re^{i\theta}) \right\}. \quad (\text{A7})$$

From this, it is clear that the combination of the vortex and the cylinder induces two image vortices of equal magnitude to the original: one at the origin, and one with opposing sign at the point $z = a^2/\bar{z}_\omega$. Now, we are interested in how this flow advects the original vortex, i.e. the form of $\mathbf{v}_{\text{flow}} = [v_r, v_\theta] = [v_r^S, v_\theta^R] + [v_r^R, v_\theta^S]$ at $z = z_\omega$, where superscripts R and S represent the irrotational and solenoidal contributions respectively. These can be calculated directly from the complex potential since

$$v_r^R = \frac{\partial\phi}{\partial r}; \quad v_r^S = -\frac{1}{r} \frac{\partial\psi}{\partial\theta}; \quad v_\theta^R = \frac{1}{r} \frac{\partial\phi}{\partial\theta}; \quad v_\theta^S = \frac{\partial\psi}{\partial r}. \quad (\text{A8})$$

Since we want to know how this flow advects the vortex, we are interested in the values of these derivatives at $r = r_\omega$ and $\theta = \theta_\omega$, and we ignore the singularity at $(r_\omega, \theta_\omega)$ because the vortex cannot self-advect. We find that the only non-zero velocity component is

$$v_\theta^S = \text{Im} \left\{ \frac{\partial w}{\partial r} \right\}_\omega = \omega \left(\frac{1}{r_\omega} - \frac{1}{r_\omega - a^2/r_\omega} \right) = \frac{\omega a^2}{r_\omega(r_\omega^2 - a^2)}, \quad (\text{A9})$$

and using distance from the boundary, $R = r_\omega - a$, and circulation for a point vortex, $\kappa = 2\pi\omega$, we obtain the desired relationship:

$$v_{\text{cyl}} = \frac{\kappa}{4\pi R} \left\{ \left(1 + \frac{r}{a}\right) \left(1 + \frac{r}{2a}\right) \right\}^{-1}. \quad (\text{A10})$$

References

- Batchelor GK. 2000. *An Introduction to Fluid Dynamics* (3rd edn). Cambridge University Press: Cambridge, UK.
- Boos WR, Hurlley JV, Murthy VS. 2015. Adiabatic westward drift of Indian monsoon depressions. *Q. J. R. Meteorol. Soc.* **141**: 1035–1048, doi: 10.1002/qj.2454.
- Chen T, Yoon J, Wang S. 2005. Westward propagation of the Indian monsoon depression. *Tellus* **57A**: 758–769.
- Dee DP, Uppala SM, Simmons AJ, Berrisford P, Poli P, Kobayashi S, Andrae U, Balmaseda MA, Balsamo G, Bauer P, Bechtold P, Beljaars ACM, van de Berg L, Bidlot J, Bormann N, Delsol C, Dragani R, Fuentes M, Geer AJ, Haimberger L, Healy SB, Hersbach H, Hólm EV, Isaksen L, Kállberg P, Köhler M, Matricardi M, McNally AP, Monge-Sanz BM, Morcrette J-J, Park BK, Peubey C, de Rosnay P, Tavolato C, Thépaut J-N, Vitart F. 2011. The ERA-Interim reanalysis: Configuration and performance of the data assimilation system. *Q. J. R. Meteorol. Soc.* **137**: 553–597, doi: 10.1002/qj.828.
- Godbole R. 1977. The composite structure of the monsoon depression. *Tellus* **29**: 25–40.
- Holland GJ. 1982. Tropical cyclone motion: Environmental interaction plus a beta effect. *J. Atmos. Sci.* **40**: 328–342.
- Hoskins BJ, James IN. 2014. *Fluid Dynamics of the Midlatitude Atmosphere*. Wiley: Chichester, UK.
- Hunt KMR, Turner AG, Inness PM, Parker DE, Levine RC. 2016. On the structure and dynamics of Indian monsoon depressions. *Mon. Weather Rev.*, doi: 10.1175/MWR-D-15-0138.1.
- Hurlley JV, Boos WR. 2015. A global climatology of monsoon low pressure system. *Q. J. R. Meteorol. Soc.* **141**: 1049–1064, doi: 10.1002/qj.2447.
- Krishnamurthy V, Ajayamohan RS. 2010. Composite structure of monsoon low pressure systems and its relation to Indian rainfall. *J. Clim.* **23**: 4285–4305, doi: 10.1175/2010JCLI2953.1.
- Krishnamurti TN. 1985. Summer monsoon experiment – a review. *Mon. Weather Rev.* **113**: 1590–1626.
- Leslie LM, Holland GJ. 1995. On the bogussing of tropical cyclones in numerical models: A comparison of vortex profiles. *Meteorol. Atmos. Phys.* **56**: 101–110.
- Milne-Thomson LM. 1940. Hydrodynamical images. *Math. Proc. Cambridge Phil. Soc.* **36**: 246–247, doi: 10.1017/S0305004100017242.
- Milne-Thomson LM. 1960. *Theoretical Hydrodynamics* (4th edn). Macmillan: London.
- Saha K, Sanders F, Shukla J. 1981. Westward propagating predecessors of monsoon depressions. *Mon. Weather Rev.* **109**: 330–343.
- Sanders F. 1984. Quasi-geostrophic diagnosis of the monsoon depression of 5–8 July 1979. *J. Atmos. Sci.* **41**: 538–552.